



Article

Tropospheric Second-Order Horizontal Gradient Modeling for GNSS PPP

Yaozong Zhou, Yidong Lou , Weixing Zhang *, Peida Wu, Jingna Bai and Zhenyi Zhang

GNSS Research Center, Wuhan University, 129 Luoyu Road, Wuhan 430079, China

* Correspondence: zhangweixing89@whu.edu.cn

Abstract: The asymmetric delay has a considerable impact on Global Navigation Satellite Systems (GNSS) Positioning, Navigation and Timing (PNT) applications. In GNSS analyses, the impacts of the asymmetric delay are commonly compensated by using the classical methods with considering the north-south and east-west horizontal gradients. In this paper, we have initiatively proposed an extended method where the north-south and east-west horizontal gradients as well as the second-order horizontal gradients are included to better fit the asymmetric delay. The modeling accuracy of the extended method was evaluated at globally distributed 905 GNSS stations during 40 days in 2020. Significant performance of the extended method respect to the classical method was found, where the hydrostatic and wet modeling accuracy at 4° elevation angle was improved from 5.3 and 10.6 mm to 1.6 and 4.9 mm by 70% and 54%, respectively. The GNSS Precise Point Positioning (PPP) performance using the extended method was also validated at 107 Multi-GNSS Experiment (MGEX) stations. The superior performance on the coordinate repeatability and significant effectiveness on the coordinate and Zenith Total Delay (ZTD) estimations were also found, and the maximal vertical (U) coordinate and ZTD difference biases reached 8.6 and −4.5 mm. The extended method is therefore recommended to substitute the classical methods in the GNSS analyses, especially under severe atmospheric conditions.

Keywords: asymmetric delay; second-order horizontal gradient; extended method; GNSS PPP



Citation: Zhou, Y.; Lou, Y.; Zhang, W.; Wu, P.; Bai, J.; Zhang, Z. Tropospheric Second-Order Horizontal Gradient Modeling for GNSS PPP. *Remote Sens.* **2022**, *14*, 4807. <https://doi.org/10.3390/rs14194807>

Academic Editors: Yunbin Yuan and Baocheng Zhang

Received: 8 September 2022

Accepted: 23 September 2022

Published: 26 September 2022

Publisher's Note: MDPI stays neutral with regard to jurisdictional claims in published maps and institutional affiliations.



Copyright: © 2022 by the authors. Licensee MDPI, Basel, Switzerland. This article is an open access article distributed under the terms and conditions of the Creative Commons Attribution (CC BY) license (<https://creativecommons.org/licenses/by/4.0/>).

1. Introduction

The electromagnetic wave signals of Global Navigation Satellite Systems (GNSS) are inevitably delayed and bent during their passage through the neutral atmosphere, generating the tropospheric Slant Total Delay (STD) that can be written as [1–5]:

$$STD(e, \alpha) = \underbrace{ZHD \cdot MF_h(e) + ZWD \cdot MF_w(e)}_{\text{isotropic part}} + \underbrace{MF_g(e) \cdot (G_n \cdot \cos(\alpha) + G_e \cdot \sin(\alpha))}_{\text{anisotropic part}} \quad (1)$$

where e and α denote elevation angle and azimuth. ZHD and ZWD represent for Zenith Hydrostatic and Wet Delay. MF_h , MF_w and MF_g stand for hydrostatic, wet and gradient mapping functions. G_n and G_e are the two horizontal gradient components in north-south and east-west directions.

The tropospheric delay can be divided into isotropic and anisotropic delays according to the azimuthal variation characteristics. The isotropic part is the product of Zenith Path Delay (ZPD) and mapping function that has been well discussed in the existing literature [6–10]. The anisotropic part is usually expressed as the function of north-south and east-west gradients based on the assumption of the tilting atmosphere, deriving the frequently used classical methods such as TANZ, CHENHER, and TILTING [11–13]. The classical methods are suitable for the asymmetry delays from the thermal expansion of the earth's atmosphere and the distribution of the atmospheric water vapor on macroscale,

while they are degraded under severe topographic perturbation or extreme weather situations, mainly due to the constraint of the simple sine and cosine structure [2].

To overcome this issue, the classical methods were extended. Gegout et al. [14] designed the Adaptive Mapping Function (AMF) based on the mapping function continued fraction and the CHENHER method, using tens of parameters to fit thousands of symmetric and asymmetric delays simultaneously, and the fitting accuracy reaches millimeter level. Masoumi et al. [15] proposed a directional model on the basis of the CHENHER method where the omni-direction is divided into several discrete azimuthal wedges and the asymmetry in each wedge is approximated independently, and the superior performance was found both in asymmetry modeling and Global Positioning System (GPS) Precise Point Positioning (PPP) under extreme weather scenarios. Landskron and Böhm [2] developed the Extended CHENHER (ECHENHER) method where the number of parameters is increased from 2 to 4, and significant improvement was also found for the modeling at low elevation angle and the Very Long Baseline Interferometry (VLBI) analyses.

However, up to now, the extended methods are all derived from the CHENHER method and focus on asymmetric modeling, lack of researches based on the more rigorous TILTING method and on the impacts of GNSS parameter estimation. In this paper, we will initiatively introduce an extended method named Extended TILTING (ETILTING) based on the ECHENHER and TILTING methods, and then systematically compare the asymmetry modeling and GNSS PPP performance of the ETILTING method. This paper is organized as follows: Section 2 describes the TANZ, CHENHER, TILTING, ECHENHER and ETILTING methods. Section 3 evaluates the asymmetry modeling performance of different methods. Section 4 compares the GNSS PPP performance by using the five modeling methods. Section 5 summarizes the work and conclusions.

2. Asymmetric Delay Modeling Methods

2.1. Classical Methods

The classical methods are all based on the tilting atmosphere assumption, and the different methods are mainly distinguished by their gradient mapping functions. MacMillan [11] proposed the TANZ method to compensate for the asymmetric effects on VLBI observations where the gradient mapping function is expressed by the product of the mapping function and $1/\tan(e)$ as:

$$AD(e, \alpha) = \frac{MF(e)}{\tan(e)} \cdot [G_n \cos(\alpha) + G_e \sin(\alpha)] \quad (2)$$

where AD denotes the Asymmetric Delay (AD). MF is the mapping function and takes MF_h , MF_w and MF_t for the hydrostatic, wet and total asymmetry modeling, respectively. Two years later, Chen and Herring [12] proposed the widely-used CHENHER method as:

$$AD(e, \alpha) = \frac{1}{\sin(e) \cdot \tan(e) + C} \cdot [G_n \cos(\alpha) + G_e \sin(\alpha)] \quad (3)$$

where C represents the gradient mapping function constant, and it takes values of 0.0031, 0.0007 and 0.0032 for the hydrostatic, wet and total asymmetry modeling, respectively. In addition, Meindl et al. [13] derived the TILTING method using the assumption of tilting zenith direction where the gradient mapping function is the derivation of MF respect to e as:

$$AD(e, \alpha) = \frac{dMF}{de} \cdot [G_n \cos(\alpha) + G_e \sin(\alpha)] \quad (4)$$

where $\frac{dMF}{de}$ is the gradient mapping function, and it takes the values of $\frac{dMF_h}{de}$, $\frac{dMF_w}{de}$ and $\frac{dMF_t}{de}$ for the hydrostatic, wet, and total modeling, respectively.

2.2. Extended Methods

The extended methods proposed by Gegout et al. [14] and Masoumi et al. [15] are too complicated to apply in operational modeling and positioning applications, and therefore only the ECHENHER and ETILTING methods will be described in this section. Landskron and Böhm [2] considered the higher-order variation of asymmetric delay and added the second-order horizontal gradients to the standard gradient formula of the CHENHER method (Equation (3)), deriving the ECHENHER method as:

$$AD(e, \alpha) = \frac{1}{\sin(e) \cdot \tan(e) + C} \cdot [G_n \cos(\alpha) + G_e \sin(\alpha) + G_{n_2} \cos(2\alpha) + G_{e_2} \sin(2\alpha)] \quad (5)$$

where G_{n_2} and G_{e_2} are the second-order horizontal gradient parameters. In this paper, we introduce the ETILTING method on the basis of the TILTING and ECHENHER methods as:

$$AD(e, \alpha) = \frac{dMF}{de} \cdot [G_n \cos(\alpha) + G_e \sin(\alpha) + G_{n_2} \cos(2\alpha) + G_{e_2} \sin(2\alpha)] \quad (6)$$

where $\frac{dMF}{de}$ denotes the gradient mapping function that can change with the atmosphere state, and it is the main advantage of the ETILTING method over the ECHENHER method. The characteristics of the extended methods are compared with the classical methods in Table 1.

Table 1. Characteristics of the classical and extended methods.

Types	Methods	Gradient Mapping Function	Higher-Order Variation	Parameters	Number of Parameters
Classical	TANZ	$\frac{MF(e)}{\tan(e)}$	×	G_n, G_e	2
	CHENHER	$\frac{1}{\sin(e) \cdot \tan(e) + C}$	×	G_n, G_e	2
	TILTING	$\frac{dMF}{de}$	×	G_n, G_e	2
Extended	ECHENHER	$\frac{1}{\sin(e) \cdot \tan(e) + C}$	✓	$G_n, G_e, G_{n_2}, G_{n_2}$	4
	ETILTING	$\frac{dMF}{de}$	✓	$G_n, G_e, G_{n_2}, G_{n_2}$	4

3. Modeling Evaluations

3.1. Modeling Strategies

We use the ray-tracing technique to retrieve hourly Slant Hydrostatic Delay (SHD) and Slant Wet Delay (SWD) from reanalysis products [16,17]. In this work, the fifth-generation Re-Analysis (ERA5) products from the European Centre for Medium-Range Weather Forecasts (ECMWF) were selected for the ray-tracing calculations [18,19], considering the superior temporal-spatial resolutions (1 h, 0.25° and 37 pressure levels) and performance [20]. The Slant Path Delays (SPDs) included SHD and SWD were retrieved at 14 elevation angles (3°, 4°, 5°, 6°, 7°, 8°, 10°, 12°, 15°, 20°, 30°, 50°, 70°, and 80°) and 16 azimuths (with an interval of 22.5°) [1,2], spanning four seasons (11–20 January, 11–20 April, 11–20 July, and 11–20 October in 2020) and covering 905 globally distributed stations as shown in Figure 1, including 549 International GNSS Service (IGS) stations and 356 stations in China.

We used the classical (TANZ, CHENHER and TILTING) and extended (ECHENHER and ETILTING) methods to model the asymmetry component of SPDs. Firstly, the asymmetric delays at 7 elevation angles (3°, 5°, 7°, 10°, 15°, 30° and 70°) and 16 azimuths (with an interval of 22.5°) were calculated by subtracting the SPD average from the SPDs at 16 azimuths [1]. Then, the modeling was performed by taking the calculated asymmetric delays as inputs and using the least-squares method where the hydrostatic and wet asymmetric

delays are modeled separately with equal weighting [1]. Finally, the five corresponding horizontal gradient models spanning 40 days and covering 905 stations were derived.

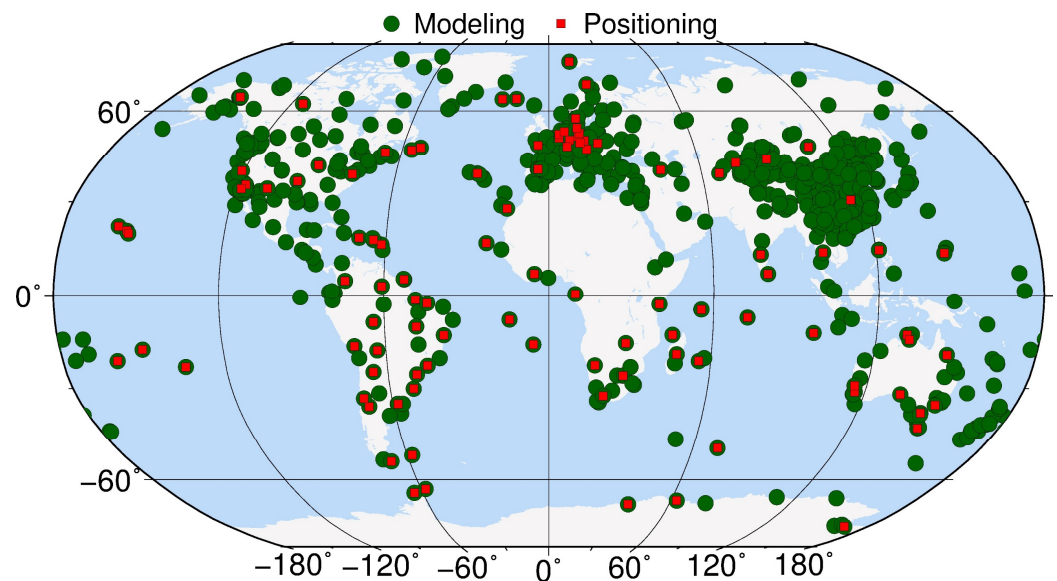


Figure 1. Distribution of the selected modeling (dark-green circles) and positioning (red squares) stations.

3.2. Modeling Residual Evaluations

In this section, we evaluate the modeling residuals using the five methods. For the evaluations, the precision index, Mean Absolute Error (MAE), was adopted [1,2,21]. The MAE at a specific elevation angle and azimuth can be calculated as:

$$MAE(e, \alpha) = |AD^o(e, \alpha) - AD^c(e, \alpha)| \quad (7)$$

where AD^o denotes the ray-traced asymmetric delay, and AD^c represents the asymmetric delay calculated from the horizontal gradient models. In this evaluation, the residual MAEs at the input modeling elevation angles and azimuths were first computed over 40 days and 905 stations. Then, the statistically residual MAEs at different modeling elevation angles were retrieved by taking the average of the MAEs at all the input azimuths and stations in 964 epochs (hours during a 40-day period) and shown in Table 2. We can find that, in the three classical methods, the TANZ method, generally with the largest residual MAEs, is obviously worst both for the hydrostatic and wet component modeling, while the CHENHER and TILTING methods show the best performance for hydrostatic and wet modeling, respectively. Compared with the classical methods, the extended methods show significant improvements at the low elevation angles ($\leq 10^\circ$) and slight degradation at the high elevation angles. The reason is that the asymmetric delays at different elevation angles are equally weighted in the modeling, and the second-order horizontal gradient estimations slightly contaminate the modeling at high elevation angles.

As shown in Table 2, the residual MAEs at 3° elevation angle are generally the largest, and, therefore, we further present the residual MAE distribution for the 905 stations at 3° elevation angle in Figure 2, where the hydrostatic and wet MAE distributions have different color bars. We can find that the MAE distribution for the three classical methods is similar (Figure 2a–c). The hydrostatic MAE distribution has latitude and topography dependence where the middle and low latitude stations around the ocean and mountains show larger MAEs, mainly due to the effects of more active atmospheric states and more severe atmospheric perturbations [22]. Compared with the hydrostatic MAE distribution, the wet MAE distribution also shows latitude and topography dependence. Several middle and low-latitude coastal areas, such as the north coast of South America, the west coast of South America, the east coast of the Mediterranean Sea, and the east of Southeast Asia,

present large MAEs, indicating the deficiencies of the classical methods. Compared with the classical methods, the extended methods show significant improvements both in MAE distribution and magnitude (Figure 2d,e). For the hydrostatic component, the latitude and topography dependence almost disappear, and the MAE magnitudes also clearly decrease. As for the wet component, although the latitude and topography dependence still exist in several regions, such as the east coast of the Mediterranean Sea and the east of Southeast Asia, the MAE is obviously smaller compared to the classical methods.

Table 2. Residual MAEs (mm) for the modeling using different methods.

Methods	Components	e = 3°	e = 5°	e = 7°	e = 10°	e = 15°	e = 30°	e = 70°
TANZ	Hydrostatic	8.78	5.01	3.64	2.23	1.14	0.31	0.04
CHENHER		8.49	3.63	2.11	1.21	0.63	0.18	0.02
TILTING		8.53	3.75	2.25	1.30	0.67	0.19	0.02
ECHENHER		2.39	1.72	1.66	1.22	0.71	0.22	0.03
ETILTING		2.45	1.92	1.80	1.29	0.74	0.22	0.03
TANZ	Wet	17.79	8.57	5.62	3.29	1.64	0.44	0.05
CHENHER		17.73	8.04	5.18	3.04	1.53	0.41	0.05
TILTING		17.67	7.55	4.66	2.70	1.36	0.37	0.04
ECHENHER		8.04	5.50	4.54	2.96	1.57	0.44	0.05
ETILTING		7.98	4.83	4.03	2.68	1.45	0.41	0.05

3.3. Modeling Accuracy Evaluations

In this section, we evaluate the modeling accuracy of different horizontal gradient models at independent elevation angles that are not involved in the modeling (4°, 6°, 8°, 12°, 20°, 50° and 80°). We first calculated the MAEs at the 905 stations and 16 azimuths in 964 epochs, and then took the average MAEs at different elevation angles and showed the statistical results in Table 3. We can also find that the CHENHER and TILTING methods perform best for hydrostatic and wet modeling, respectively. The extended methods obviously have better performance both for the hydrostatic and wet components at low elevation angles, and the maximal improvement exceeds 6 mm. As for the two extended methods, the ECHENHER method is slightly better for hydrostatic modeling, and the ETILTING method has better wet modeling performance with a maximal improvement of about 0.62 mm.

Table 3. MAEs (mm) for the modeling using different methods.

Methods	Components	e = 4°	e = 6°	e = 8°	e = 12°	e = 20°	e = 50°	e = 80°
TANZ	Hydrostatic	5.81	4.30	3.08	1.67	0.68	0.11	0.03
CHENHER		5.27	2.69	1.71	0.91	0.39	0.07	0.02
TILTING		5.31	2.84	1.84	0.97	0.41	0.07	0.02
ECHENHER		1.51	1.76	1.52	0.98	0.45	0.08	0.02
ETILTING		1.63	1.93	1.62	1.02	0.47	0.08	0.03
TANZ	Wet	11.14	6.89	4.64	2.43	0.97	0.15	0.03
CHENHER		10.84	6.37	4.28	2.25	0.90	0.14	0.03
TILTING		10.64	5.81	3.82	2.00	0.81	0.13	0.03
ECHENHER		5.31	5.13	3.95	2.26	0.95	0.15	0.03
ETILTING		4.91	4.51	3.53	2.07	0.88	0.14	0.03

The modeling MAEs using different methods are generally largest at 4° elevation angle, and the MAE distribution for the 905 stations is therefore presented at 4° elevation angle in Figure 3. We can find that the classical methods have similar MAE distributions (Figure 3a–c). The hydrostatic MAE distribution is correlated with the station latitudes, and the middle and low latitude areas with more active hydrostatic atmosphere states show larger MAEs [22]. In addition, the MAE distribution also depends on the topography to

some degree, and some sea and land boundary areas show much larger MAEs. The wet MAE distribution also shows obvious latitude and topography dependence, and several coastal areas, such as the north and west coasts of South America and eastern areas of Southeast Asia, have much larger MAEs. In contrast, the MAE distribution of the extended methods is much better (Figure 3d,e), where latitude and topography dependence are not obvious anymore.

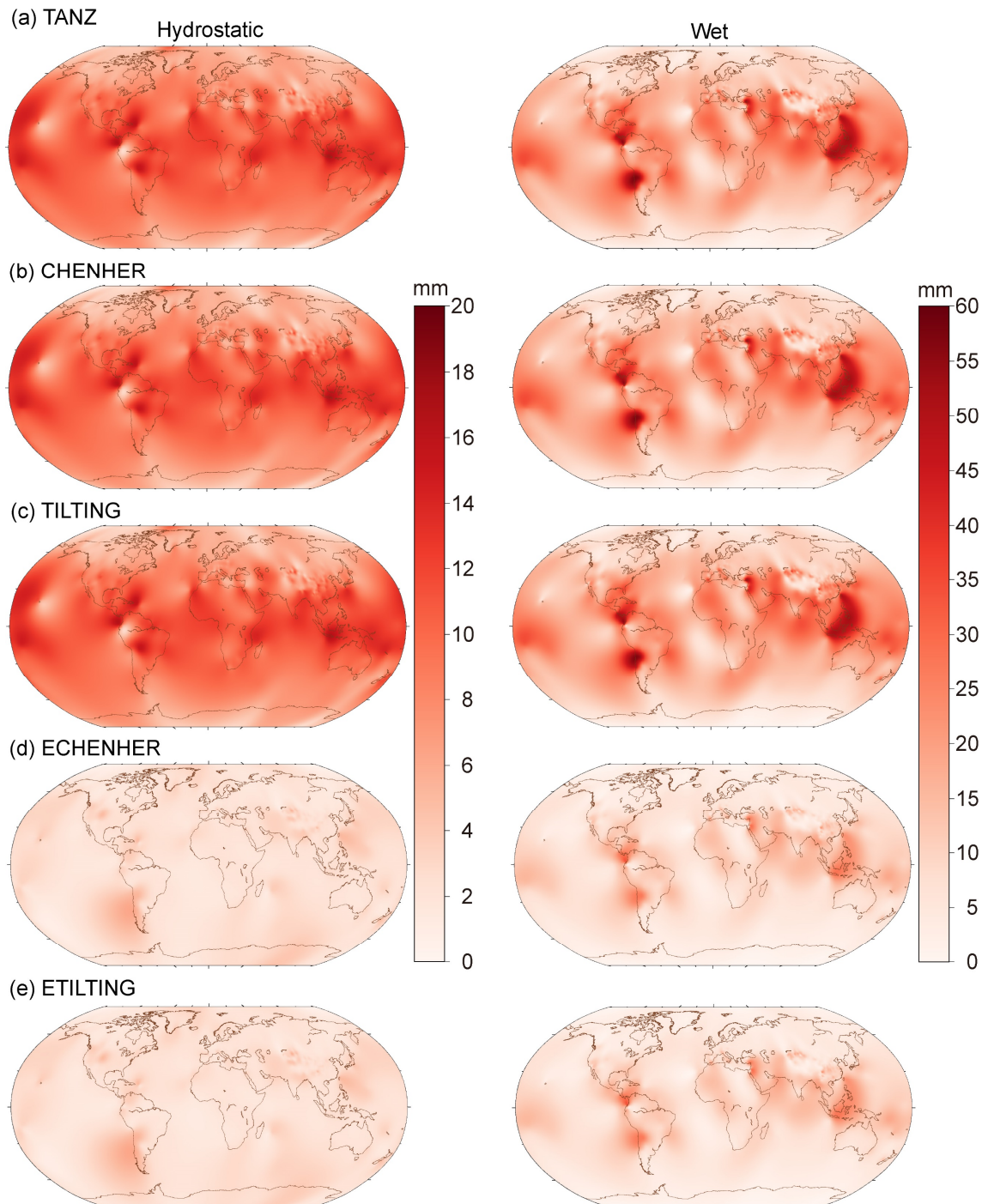


Figure 2. Residual MAE distribution at 3° elevation angle for the hydrostatic (left) and wet (right) modeling by using the TANZ (a), CHENHER (b), TILTING (c), ECHENHER (d) and ETILTING (e) methods.

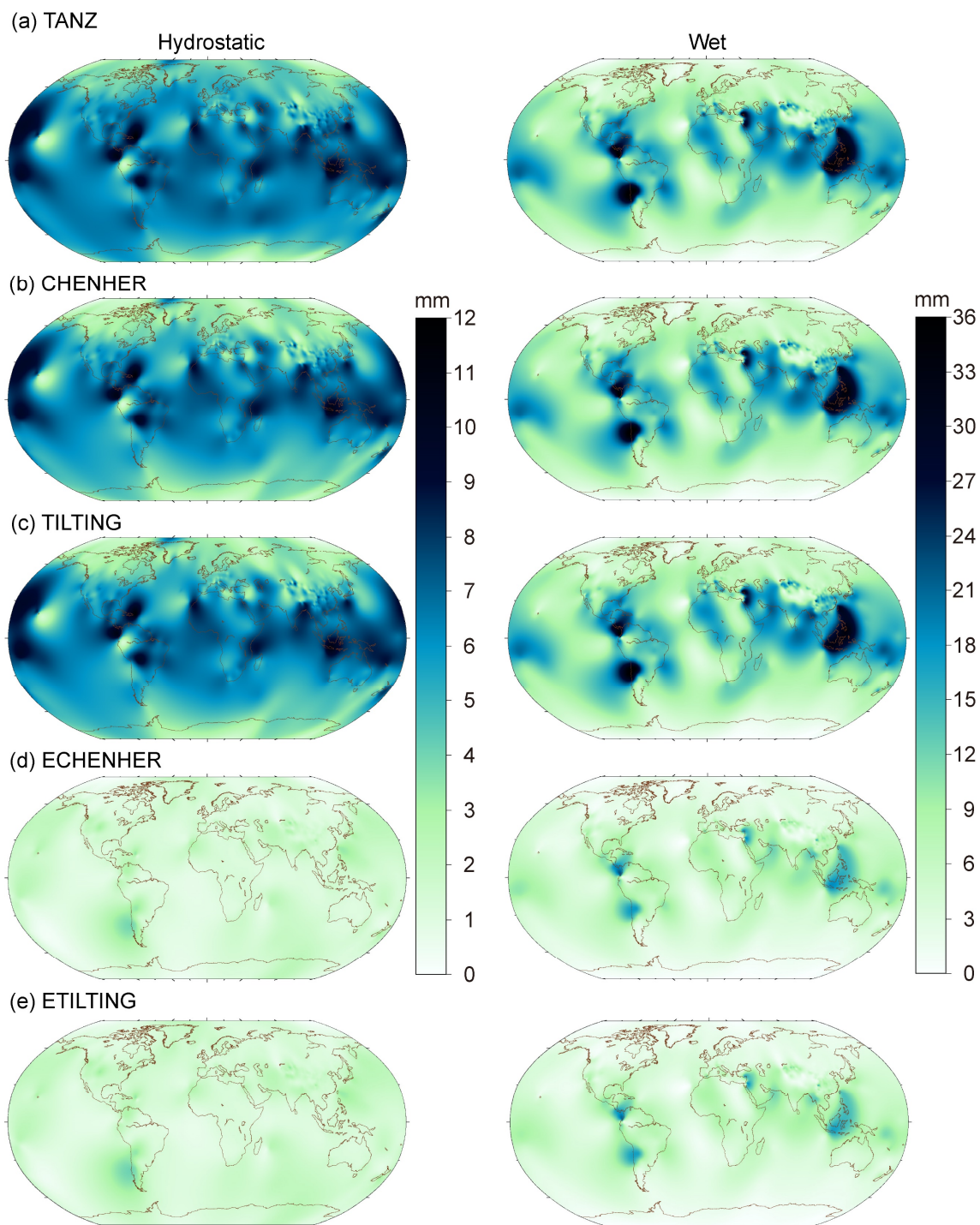


Figure 3. MAE distribution at 4° elevation angle for the hydrostatic (left) and wet (right) modeling by using the TANZ (a), CHENHER (b), TILTING (c), ECHENHER (d) and ETILTING (e) methods.

4. GNSS PPP Validations

4.1. Data Processing Strategies

In operational GNSS analyses, the effects of asymmetric delay are generally modeled by the north-south and east-west gradient estimations using the classical method. In this section, we initiatively use the extended method instead of the classical method for horizontal gradient estimations considering the better modeling accuracy and compare the multi-GNSS PPP performances of different methods. There are three classical methods (TANZ, CHENHER, and TILTING) and two extended methods (ECHENHER and

ETILTING) involved in the GNSS analyses, where the classical methods estimate the G_n and G_e parameters, and the extended methods additionally include the two second-order horizontal gradient parameters (G_{n_2} and G_{e_2}). In addition, the multi-GNSS PPP with no horizontal estimations (NONE) is also performed. Therefore, a total of six PPP schemes will be included in this section.

We use the Positioning and Navigation Data Analyst (PANDA) software [23] to analyze the multi-GNSS (GPS+GLONASS+GALILEO+BDS3) data from 107 globally distributed IGS Multi-GNSS Experiment (MGEX) stations as shown in Figure 1 [24], and the time period is from 11–20 October in 2020. The satellite orbits are fixed by the German Research Center for Geosciences (GFZ) GBM products, and the satellite clock corrections are estimated every 5 min using the corresponding schemes to the PPP processing to avoid the influence of inconsistency. The detailed processing strategies for the six PPP schemes are listed in Table 4.

Table 4. Data processing strategies for multi-GNSS PPP.

Observation	Sampling interval	300 s
	Frequency combination	Ionosphere-free combination
	Elevation cutoff angle	3°
	Satellite system weighting factors	GPS: 1; GALILEO: 1; GLONASS: 1.5; BDS MEO and IGSO: 1.5; BDS GEO: 2.5
	Elevation weighting strategy	$\begin{cases} p = 2\text{sine}, (e \leq 30^\circ) \\ p = 1, (e > 30^\circ) \end{cases}$
Error correction	Phase center variations	igs14.atx
	Higher-order ionospheric delay	GIM and IGRF13 [25]
	Ocean tide loading	FES2014b
	A priori tropospheric delay	MFlsmcom+ZPD [10]
Parameter estimation	Satellite orbits	Fixed from GBM 5 min products
	Satellite clock corrections	Fixed from estimated 5 min products
	Mapping function	Wet MFlsmcom [10]
	ZWD stochastic model	Piece-wise constant (1 h), random walk between segments (15mm/ \sqrt{h})
	Gradient mapping function	Scheme 1 NONE: NONE Scheme 2 TANZ: $m f_w \cdot \cot(e)$ Scheme 3 CHENHER: $\frac{1}{\sin(e) \cdot \tan(e) + 0.0032}$ Scheme 4 TILTING: $\frac{dMF_w}{de}$ Scheme 5 ECHENHER: $\frac{1}{\sin(e) \cdot \tan(e) + 0.0032}$ Scheme 6 ETILTING: $\frac{dMF_w}{de}$
	Gradient stochastic model	Piece-wise constant (2 h), random walk between segments (10mm/ \sqrt{h})
	Horizontal gradient	Scheme 1 NONE: NONE Scheme 2 TANZ: G_{n_1}, G_{e_1} Scheme 3 CHENHER: G_{n_1}, G_{e_1} Scheme 4 TILTING: G_{n_1}, G_{e_1} Scheme 5 ECHENHER: $G_{n_1}, G_{e_1}, G_{n_2}, G_{e_2}$ Scheme 6 ETILTING: $G_{n_1}, G_{e_1}, G_{n_2}, G_{e_2}$
	Station coordinates	Daily constant
	Receiver clock corrections	White noise
	Ambiguities	Fixed

4.2. Coordinate Repeatability

In this section, we compare the coordinate repeatability of the six PPP schemes. We first extracted the 10-day coordinate time series from the PPP daily solutions and then removed the effect of Atmospheric Pressure Loading (APL) on the time series by using the APL products from Technische Universität Wien [26,27]. After that, we calculated the coordinate repeatability without and with APL correction as shown in Table 5.

Table 5. Coordinate repeatability (mm) for the six PPP schemes.

Schemes	Without APL Correction			With APL Correction		
	N	E	U	N	E	U
NONE	1.82	1.48	4.10	1.84	1.52	3.83
TANZ	0.92	0.88	3.39	0.95	0.94	3.10
CHENHER	0.91	0.88	3.41	0.94	0.94	3.13
TILTING	0.91	0.87	3.40	0.94	0.94	3.11
ECHENHER	0.89	0.85	3.37	0.93	0.90	3.09
ETILTING	0.88	0.84	3.35	0.92	0.89	3.06

We can find that the APL correction improves the vertical (U) coordinate repeatability by about 0.3 mm with slightly contaminating the North (N) and East (E) components. The six PPP schemes have different performances in which the PPP scheme without gradient estimation (NONE) shows the worst repeatability, with a standard deviation of 1.84, 1.52 and 3.83 mm in the N, E and U directions, respectively. Compared with the NONE scheme, the schemes using the three classical methods show improvements reaching about 0.9, 0.6 and 0.7 mm on average. As for the extended methods, the coordinate repeatability is further improved by about 0.02, 0.05 and 0.05 mm, showing the advantages of estimating the second-order horizontal gradients. While for the schemes using different classical methods or extended methods, the coordinate repeatability is very close in which the TILTING and ETILTING schemes are slightly better than the CHENHER and ECHENER schemes. However, the coordinate repeatability differences between different schemes are not as significant as the modeling accuracy differences, and the main reason is that the modeling accuracy differences are concentrated on the low elevation angles, which are greatly suppressed by the elevation-dependent weighting strategy.

In addition to the statistical coordinate repeatability, the coordinate repeatability difference distribution between the TILTING and ECHENHER schemes and the ETILTING scheme is also shown in Figure 4, where the red color represents that the TILTING and ECHENHER schemes are worse than the ETILTING scheme. We can find that the coordinate repeatability differences between the TILTING and ETILTING schemes are obviously larger than those between the ECHENER and ETILTING schemes, demonstrating that the impact of the number of horizontal gradient parameters to be estimated is larger than the gradient mapping functions. In all 107 stations, there are 59, 69 and 60 stations with better N, E and U coordinate repeatability for the ETILTING scheme than for the TILTING scheme, again indicating the superior performance of the ETILTING method (left column of Figure 4). The U coordinate repeatability differences are most remarkable in the three coordinate components, and some middle and low latitude stations around the ocean show more significant differences with the maximal value of 2.32 mm (left column of Figure 4c) that is consistent with the modeling accuracy distribution.

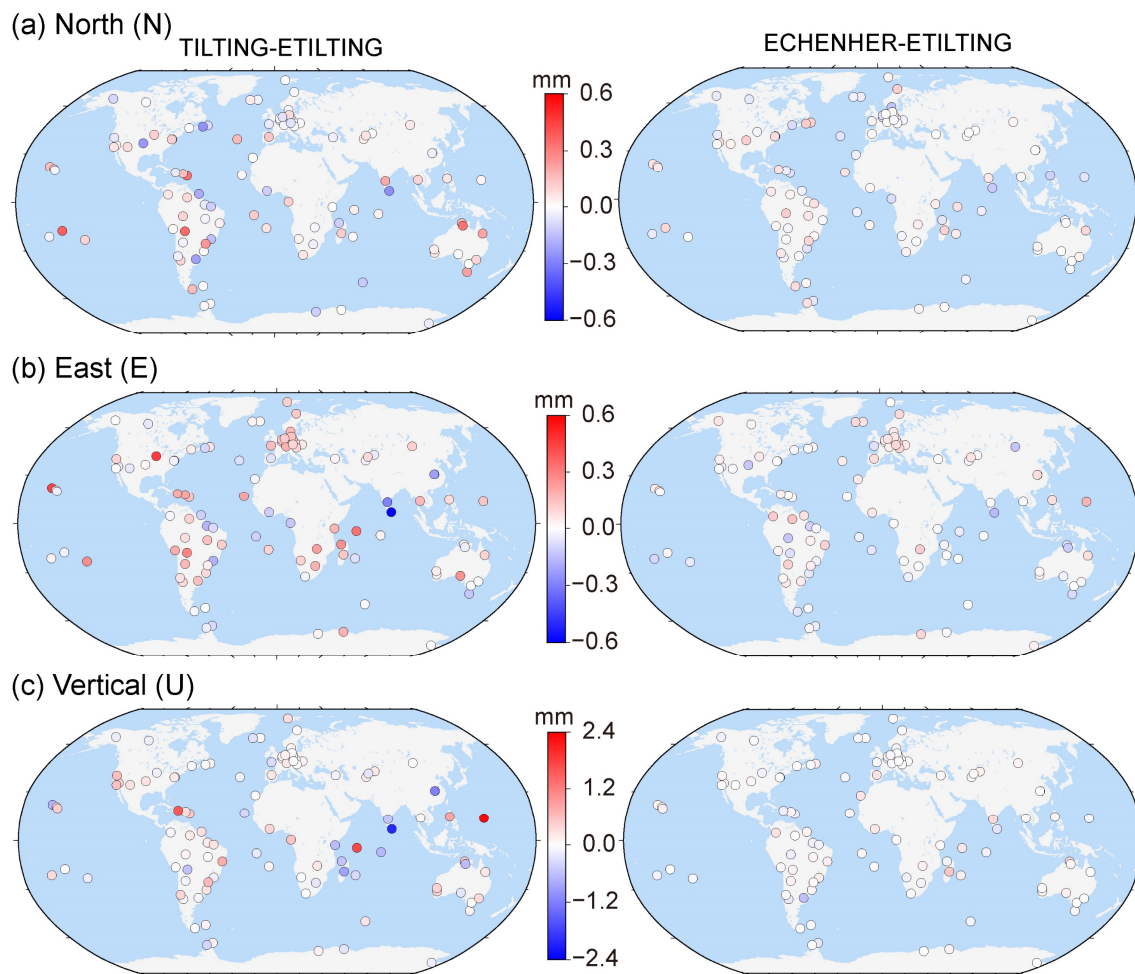


Figure 4. Distribution of north (a), east (b) and vertical (c) coordinate repeatability differences between the TILTING (left) and ECHENHER (right) schemes and the ETILTING scheme.

4.3. Coordinate and ZTD Differences

The coordinate repeatability cannot reflect the potential systematic bias in the position time series. Therefore, we further analyzed the coordinate and Zenith Total Delay (ZTD) differences between the TILTING, ECHENHER and TILTING schemes, where the statistical difference bias and Root Mean Square (RMS) are summarized in Table 6. We can find that the coordinate and ZTD differences between the TILTING and ETILTING schemes are also more significant than the differences between the ECHENHER and ETILTING schemes, illustrating the effectiveness of the second-order horizontal gradient estimation. Among all the statistical components, the U coordinate and ZTD differences are larger than the horizontal component differences, and the biases are 0.49 and -0.19 mm, respectively, indicating the potential systemic biases between the TILTING and ETILTING schemes.

Table 6. Coordinate and ZTD differences (mm) between the TILTING and ECHENHER schemes and the ETILTING scheme.

Components	TILTING-ETILTING		ECHENHER-ETILTING	
	Bias	RMS	Bias	RMS
N	-0.04	0.36	0.01	0.16
E	-0.07	0.44	0.02	0.18
U	0.49	1.45	-0.01	0.39
ZTD	-0.19	0.99	-0.01	0.30

In order to further illustrate the potential systematic bias, we plotted the bias and RMS distribution of the coordinate and ZTD differences between the TILTING and ETILTING schemes in Figure 5. We can find that the horizontal coordinate difference bias and RMS are smaller than the U coordinate and ZTD. The U coordinate difference biases have the opposite sign to ZTD, and the magnitudes are generally double those of the ZTD biases, indicating the strong correlation between U coordinate and ZTD [28]. The U coordinate and ZTD difference biases also depend on the station latitude, and the stations located in the middle and low latitudes generally show larger values, such as WUH2 (China) and NLIB (North America). At the two stations, the U coordinate and ZTD difference biases are nearly equal to the corresponding RMSs, indicating the significant systematic biases between the TILTING and ETILTING schemes. Considering the prominent biases, we further presented the coordinate and ZTD difference time series in Figure 6. We can find that the coordinate and ZTD difference time series between the two schemes are consistently positive or negative, with the statistical N, E, U, and ZTD difference biases of -1.08 , 1.56 , 8.61 and -4.47 mm for NLIB station, and of -2.53 , 1.10 , 5.10 and -3.02 mm for WUH2 station, demonstrating the significant effectiveness of the proposed ETILTING method relative to the TILTING method.

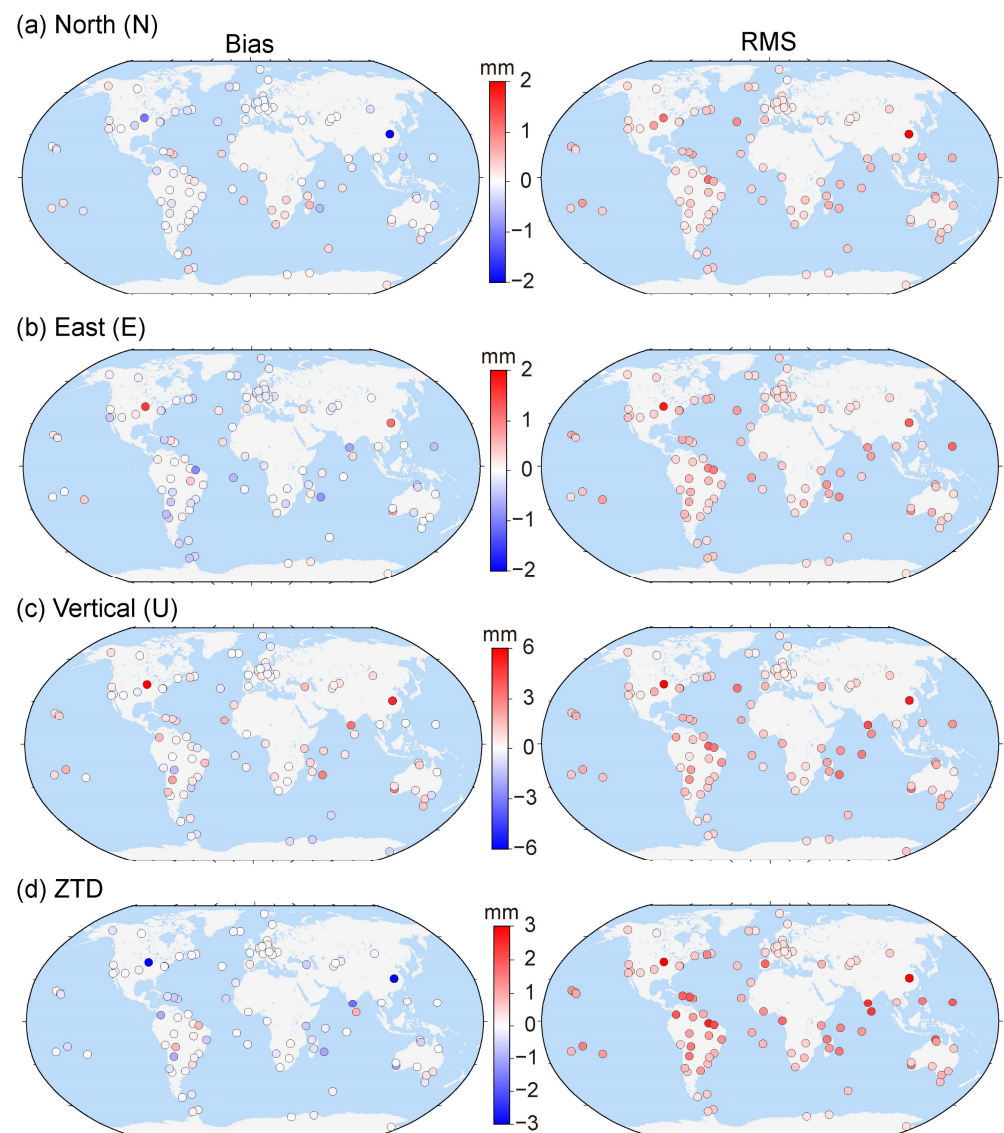


Figure 5. Bias (left) and RMS (right) distribution of north (a), east (b) and vertical (c) coordinates and ZTD (d) differences between the TILTING and ETILTING schemes.

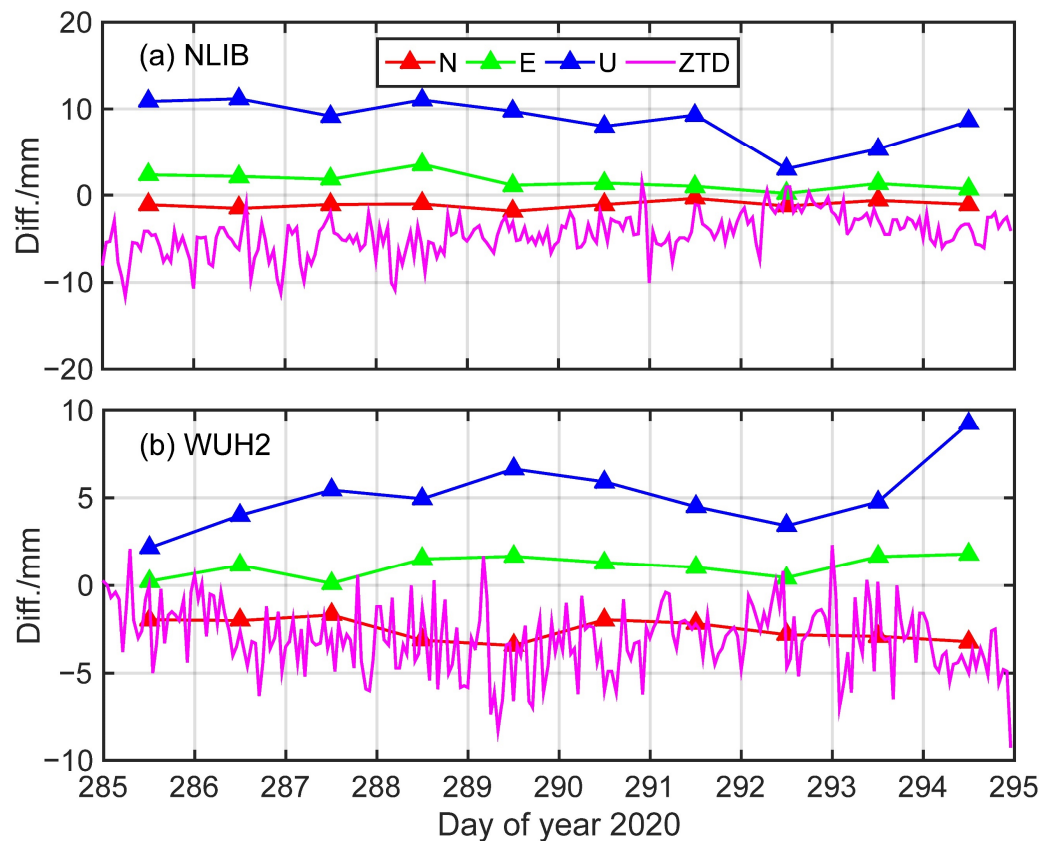


Figure 6. Coordinate and ZTD difference time series between the TILTING and ETILTING schemes at NLIB (a) and WUH2 (b) stations.

5. Conclusions

The asymmetric delays have non-negligible impacts on GNSS analyses. In the past decades, several classical methods, such as TANZ, CHENHER and TILTING, were proposed for better eliminating the impacts. However, limited by the simple sine and cosine structures, the classical methods perform poorly under the atmospheric state with severe variation. To deal with the issue, more sophisticated extended methods were introduced. In this paper, we reviewed the existing classical and extended methods and initiatively proposed a new extended method named ETILTING. The modeling residual and accuracy of the existing methods and the ETILTING method at 905 GNSS stations during 40 days in 2020 were evaluated. We found that the extended methods show very significant improvements to the classical methods both for the modeling residual and accuracy, where the hydrostatic and wet modeling accuracy of the ETILTING method at 4° elevation angle is improved from 5.3 and 10.6 mm of the TILTING method to 1.6 and 4.9 mm by 70% and 54%, respectively. As for the extended methods, the ETILTING method shows better performance than the ECHENHER method, and the maximal improvement in the modeling accuracy reaches 0.62 mm.

In addition, the multi-GNSS PPP performance of different methods was also validated at 107 MGEX stations. The coordinate repeatability as well as the coordinate and ZTD differences were systematically compared. The results show that the PPP scheme using the ETILTING method can improve the N, E, and U coordinates repeatability from 0.94, 0.94 and 3.11 mm to 0.92, 0.89 and 3.06 mm, indicating the superior performance of the ETILTING method to the TILTING method. In addition, the significant U coordinate and ZTD biases between the schemes using the TILTING and ETILTING methods were also found, and the maximum U coordinate and ZTD difference biases reached 8.6 and -4.5 mm, illustrating the effectiveness of the ETILTING method. In brief, the extended

methods have better accuracy and PPP performance. We recommend the extended methods to substitute the frequently-used classical methods in the GNSS analyses, especially under severe atmospheric conditions.

Author Contributions: Conceptualization, Y.Z., Y.L. and W.Z.; methodology, Y.Z., W.Z. and Y.L.; software, Y.Z. and W.Z.; validation, Y.Z., W.Z. and Y.L.; formal analysis, Y.Z. and W.Z.; investigation, Y.Z. and W.Z.; resources, Y.Z., P.W., J.B. and Z.Z.; data curation, Y.Z., J.B. and Z.Z.; writing—original draft preparation, Y.Z.; writing—review and editing, Y.L., W.Z. and Y.Z.; visualization, Y.Z.; supervision, Y.L. and W.Z.; project administration, Y.L. and W.Z.; funding acquisition, Y.L. and W.Z. All authors have read and agreed to the published version of the manuscript.

Funding: This work was supported by the National Natural Science Foundation of China (42174027); Key Research and Development Program of Guangxi Zhuang Autonomous Region, China (2020AB44004); the Fundamental Research Funds for the Central Universities (2042022kf1198).

Data Availability Statement: ERA5 was downloaded from Copernicus Climate Data Store (<https://cds.climate.copernicus.eu/>) (accessed on 7 September 2022). IGS MGEX RINEX data and GFZ GBM satellite orbit product are available through IGS CDDIS FTP (<https://gdc.cddis.eosdis.nasa.gov/>) (accessed on 7 September 2022) and GFZ FTP (<ftp://ftp.gfz-potsdam.de/>) (accessed on 7 September 2022). APL products was downloaded from Technische Universität Wien (<http://vmf.geo.tuwien.ac.at/>) (accessed on 7 September 2022).

Acknowledgments: Authors would like to thank Copernicus Climate Data Store, IGS CDDIS and GFZ for providing the research datasets and products, and acknowledge Technische Universität Wien for releasing APL products. The numerical calculations in this paper have been done on the supercomputing system in the Supercomputing Center of Wuhan University.

Conflicts of Interest: The authors declare no conflict of interest.

References

1. Landskron, D. Modeling Tropospheric Delays for Space Geodetic Techniques. Doctoral Dissertation, Department of Geodesy and Geoinformation, TU Wien, Vienna, Austria, 2017. Supervisor: Böhm J. Available online: <http://repositum.tuwien.ac.at/obvutwhs/content/titleinfo/2099559> (accessed on 7 September 2022).
2. Landskron, D.; Böhm, J. Refined discrete and empirical horizontal gradients in VLBI analysis. *J. Geod.* **2018**, *92*, 1387–1399. [[CrossRef](#)]
3. Liu, J.; Gao, K.; Guo, W.; Cui, J.; Guo, C. Role, path, and vision of “5G + BDS/GNSS”. *Satell. Navig.* **2020**, *1*, 23. [[CrossRef](#)]
4. Huang, L.; Zhu, G.; Liu, L.; Chen, H.; Jiang, W. A global grid model for the correction of the vertical zenith total delay based on a sliding window algorithm. *GPS Solut.* **2021**, *25*, 98. [[CrossRef](#)]
5. Huang, L.; Chen, H.; Liu, L.; Jiang, W. A new high-precision global model for calculating zenith tropospheric delay. *Chin. J. Geophys.-CH* **2021**, *64*, 782–795. [[CrossRef](#)]
6. Zhu, G.; Huang, L.; Liu, L.; Li, C.; Li, J.; Huang, L.; Zhou, L.; He, H. A new approach for the development of grid models calculating tropospheric key parameters over China. *Remote Sens.* **2021**, *13*, 3546. [[CrossRef](#)]
7. Huang, L.; Zhu, G.; Peng, H.; Chen, H.; Liu, L.; Jiang, W. A global grid model for the vertical correction of zenith wet delay based on the sliding window algorithm. *Acta Geod. Cartogr. Sin.* **2021**, *50*, 685–694. [[CrossRef](#)]
8. Böhm, J.; Werl, B.; Schuh, H. Troposphere mapping functions for GPS and very long baseline interferometry from European Centre for Medium-Range Weather Forecasts operational analysis data. *J. Geophys. Res. Solid Earth* **2006**, *111*, 1–9. [[CrossRef](#)]
9. Landskron, D.; Böhm, J. VMF3/GPT3: Refined discrete and empirical troposphere mapping functions. *J. Geod.* **2018**, *92*, 349–360. [[CrossRef](#)]
10. Zhou, Y.; Lou, Y.; Zhang, W.; Bai, J.; Zhang, Z. An improved tropospheric mapping function modeling method for space geodetic techniques. *J. Geod.* **2021**, *95*, 98. [[CrossRef](#)]
11. MacMillan, D. Atmospheric gradients from very long baseline interferometry observations. *Geophys. Res. Lett.* **1995**, *22*, 1041–1044. [[CrossRef](#)]
12. Chen, G.; Herring, T. Effects of atmospheric azimuthal asymmetry on the analysis of space geodetic data. *J. Geophys. Res. Solid Earth* **1997**, *102*, 20489–20502. [[CrossRef](#)]
13. Meindl, M.; Schaer, S.; Hugentobler, U.; Beutler, G. Tropospheric gradient estimation at CODE: Results from global solutions. *J. Meteorol. Soc. JPN* **2004**, *82*, 331–338. [[CrossRef](#)]
14. Gegout, P.; Biancale, R.; Soudarin, L. Adaptive mapping functions to the azimuthal anisotropy of the neutral atmosphere. *J. Geod.* **2011**, *85*, 661–677. [[CrossRef](#)]
15. Masoumi, S.; McClusky, S.; Koulali, A.; Tregoning, P. A directional model of tropospheric horizontal gradients in Global Positioning System and its application for particular weather scenarios. *J. Geophys. Res. Atmos.* **2017**, *122*, 4401–4425. [[CrossRef](#)]

16. Hofmeister, A. Determination of Path Delays in the Atmosphere for Geodetic VLBI by Means of Ray-Tracing. Doctoral Dissertation, Department of Geodesy and Geoinformation, TU Wien, Vienna, Austria, 2016. Supervisor: Böhm J. Available online: <http://resolver.obvsg.at/urn:nbn:at:at-ubtuw:1-3444> (accessed on 7 September 2022).
17. Hofmeister, A.; Böhm, J. Application of ray-traced tropospheric slant delays to geodetic VLBI analysis. *J. Geod.* **2017**, *91*, 945–964. [[CrossRef](#)] [[PubMed](#)]
18. Hersbach, H.; Bell, B.; Berrisford, P. The ERA5 global reanalysis. *Q. J. Roy. Meteor. Soc.* **2020**, *146*, 1999–2049. [[CrossRef](#)]
19. Huang, L.; Wang, X.; Xiong, S.; Li, J.; Liu, L.; Mo, Z.; Fu, B.; He, H. High-precision GNSS PWV retrieval using dense GNSS sites and in-situ meteorological observations for the evaluation of MERRA-2 and ERA5 reanalysis products over China. *Atmos. Res.* **2022**, 106247. [[CrossRef](#)]
20. Zhou, Y.; Lou, Y.; Zhang, W.; Kuang, C.; Liu, W.; Bai, J. Improved performance of ERA5 in global tropospheric delay retrieval. *J. Geod.* **2020**, *94*, 103. [[CrossRef](#)]
21. Urquhart, L.; Nievinski, F.G.; Santos, M.C. Assessment of troposphere mapping functions using three-dimensional ray-tracing. *GPS Solut.* **2014**, *18*, 345–354. [[CrossRef](#)]
22. Nikolaidou, T.; Balidakis, K.; Nievinski, F.G.; Santos, M.C.; Schuh, H. Impact of different NWM-derived mapping functions on VLBI and GPS analysis. *Earth Planets Space* **2018**, *70*, 95. [[CrossRef](#)]
23. Shi, C.; Zhao, Q.; Geng, J.; Lou, Y.; Ge, M.; Liu, J. Recent development of PANDA software in GNSS data processing. In *International Conference on Earth Observation Data Processing and Analysis (ICEODPA)*; International Society for Optics and Photonics: Bellingham, WA, USA, 2008; Volume 7285, p. 72851S. [[CrossRef](#)]
24. Montenbruck, O.; Steigenberger, P.; Prange, L.; Deng, Z.; Zhao, Q.; Perosanz, F.; Romero, I.; Noll, C.; Stürze, A.; Weber, G. The Multi-GNSS Experiment (MGEX) of the International GNSS Service (IGS)—achievements, prospects and challenges. *Adv. Space Res.* **2017**, *59*, 1671–1697. [[CrossRef](#)]
25. Fritsche, M.; Dietrich, R.; Knöfel, C.; Rülke, A.; Vey, S.; Rothacher, M.; Steigenberger, P. Impact of higher-order ionospheric terms on GPS estimates. *Geophys. Res. Lett.* **2005**, *32*, 1–5. [[CrossRef](#)]
26. Tregoning, P.; Dam, T.V. Atmospheric pressure loading corrections applied to GPS data at the observation level. *Geophys. Res. Lett.* **2005**, *32*, 1–4. [[CrossRef](#)]
27. Wijaya, D.D.; Böhm, J.; Karbon, M.; Kràsna, H.; Schuh, H. Atmospheric pressure loading. In *Atmospheric Effects in Space Geodesy*; Springer: Berlin/Heidelberg, Germany, 2013; pp. 137–157. Available online: <https://link.springer.com/book/10.1007/978-3-642-36932-2> (accessed on 7 September 2022).
28. Tregoning, P.; Herring, T.A. Impact of a priori zenith hydrostatic delay errors on GPS estimates of station heights and zenith total delays. *Geophys. Res. Lett.* **2006**, *33*, 1–5. [[CrossRef](#)]